

Enhanced Laterally Resolved ToF-SIMS and AFM Imaging of the  
Electrically Conductive Structures in Cable Bacteria

Peer-reviewed author version

THIRUVALLUR EACHAMBADI, Ragha; Boschker, Henricus; Franquet, Alexis;  
Spampinato, Valentina; Hidalgo-Martinez, Silvia; VALCKE, Roland; Meysman, Filip &  
MANCA, Jean (2021) Enhanced Laterally Resolved ToF-SIMS and AFM Imaging of  
the Electrically Conductive Structures in Cable Bacteria. In: ANALYTICAL  
CHEMISTRY, 93(19), p.7226-7234.

DOI: 10.1021/acs.analchem.1c00298

Handle: <http://hdl.handle.net/1942/34020>

# Enhanced laterally resolved ToF-SIMS and AFM imaging of the electrically conductive structures in cable bacteria

Raghavendran Thiruvallur Eachambadi<sup>[a]</sup>, Henricus T. S. Boschker<sup>[b], [c]</sup>, Alexis Franquet<sup>[d]</sup>, Valentina Spampinato<sup>[d]</sup>, Silvia Hidalgo-Martinez<sup>[c]</sup>, Roland Valcke<sup>[e]</sup>, Filip J. R. Meysman<sup>[c], [b]</sup>, Jean V. Manca<sup>[a]\*</sup>

[a] UHasselt – X-LAB, Agoralaan, 3590 Diepenbeek, Belgium

[b] Department of Biotechnology, Delft University of Technology, Van der Maasweg 9, 2629 HZ Delft, The Netherlands

[c] Department of Biology, University of Antwerp, Universiteitsplein 1, 2610 Wilrijk, Belgium

[d] Materials and Components Analysis – Compositional Analysis, Imec vzw, Kapeldreef 75, 3001 Leuven, Belgium

[e] UHasselt – Molecular and Physical Plant Physiology, Agoralaan, 3590 Diepenbeek, Belgium

\*Email: jean.manca@uhasselt.be

---

**ABSTRACT:** Cable bacteria are electroactive bacteria that form a long, linear chain of ridged cylindrical cells. These filamentous bacteria perform centimeter-scale long-range electron transport through parallel, interconnected conductive pathways of which the detailed chemical and electrical properties are still unclear. Here, we combine ToF-SIMS (time of flight secondary ion mass spectrometry) and AFM (atomic force microscopy) to investigate the structure and composition of this naturally-occurring electrical network. The enhanced lateral resolution achieved allows differentiation between the cell body and the cell-cell junctions that contain a conspicuous cartwheel structure. Three ToF-SIMS modes were compared in the study of so-called fiber sheaths (i.e., the cell material that remains after removal of cytoplasm and membranes and which embeds the electrical network). Among these, fast imaging delayed extraction (FI-DE) was found to balance lateral and mass resolution, thus yielding multiple benefits in the study of structure-composition relations in cable bacteria: (i) it enables the separate study of the cell body and cell-cell junctions, (ii) by combining FI-DE with *in-situ* AFM, the depth of Ni-containing protein – key in the electrical transport – is determined with greater precision, and (iii) this combination prevents contamination, which is possible when using an *ex-situ* AFM. Our results imply that the interconnects in extracted fiber sheaths are either damaged during extraction, or that their composition is different from fibers, or both. From a more general analytical perspective, the proposed methodology of ToF-SIMS in FI-DE-mode combined with *in-situ* AFM holds great promise for studying the chemical structure of other biological systems.

---

Cable bacteria are multicellular microorganisms that form long branched filaments and belong to the *Desulfobulbaceae* family<sup>1</sup>. They are the focus of interdisciplinary research due to their unique capability of conducting electrical currents over centimeter distances<sup>2,3</sup>, a process also known as long-distance electron transport (LDET). Cable bacteria have been found to thrive in different environments such as fresh water<sup>4,5</sup> and marine sediments<sup>6,7</sup> and have also been found in different parts of the world<sup>7</sup>. Cable bacteria display a distinct morphology with parallel ridges running along the length of the filament<sup>1,8,9</sup>. Scanning Electron Microscopy of cable bacteria cross-sections revealed the presence of fibers of about 50 nm in diameter under the ridges and a cartwheel structure at the junctions<sup>8</sup>. These fibers are embedded in the periplasm (i.e., in space between the cytoplasmic membrane and the bacterial outer membrane) and were suspected to be the conductive structures<sup>8</sup> (Figure 1 A-C).

Recently, Meysman et al. experimentally investigated the conductivity of these fibers<sup>9</sup>. A sequential extraction procedure was developed<sup>8</sup> (see experimental section), by which the fiber structures can be isolated from cable bacterium filaments<sup>8</sup>. After chemical removal of cytoplasm and membranes, a so-called fiber sheath remains, which embeds the periplasmic fibers<sup>9-11</sup>. The fiber sheath flattens when air-dried (Figure 1D), and the top part of this fiber sheath mirrors the bottom part due to its cylindrical symmetry<sup>8</sup>.

Meysman et al. demonstrated that fibers sheaths were indeed highly conductive<sup>9</sup>. Fiber sheaths were placed on top of two gold pads with a

non-conductive oxide spacing, and when applying a potential difference between the two pads, a flow of current indicated that the periplasmic fibers are the conductive conduits. These results were subsequently confirmed with conductive atomic force microscopy (C-AFM)<sup>10</sup>. The conductivity of these periplasmic fibers (> 20 S/cm) not only rivals that of doped organic semiconductors<sup>9</sup>, but the length scale of electron transport is also more than three orders of magnitude longer than previously known for microbial structures<sup>3</sup>. Therefore, there is a strong interest in this material for future biodegradable electronic applications.

In order to better understand the unique electrical properties of cable bacteria, a key challenge is to unravel the composition of the electrically conductive fibers. Here, we combine ToF-SIMS and AFM to investigate the structure and composition of this natural-occurring electrical network of fibers with enhanced lateral resolution. Mass spectrometry-based chemical imaging is widely used for different types of cellular analyses<sup>12-14</sup>. Various SIMS techniques are available, of which ToF-SIMS and nanoscale secondary ion mass spectrometry (NanoSIMS) are routinely utilized. Of the two, NanoSIMS provides the best lateral resolution (< 50 nm), but is limited in the number of elemental masses that can be simultaneously detected<sup>15-19</sup>. With isotopic labelling, NanoSIMS can be used to localize the incorporation of different elements (C, N, S) within the cell compartments<sup>20-22</sup>, and this technique has also been recently applied to cable bacteria to investigate the relation between LDET metabolism and filament growth<sup>20-22</sup>.

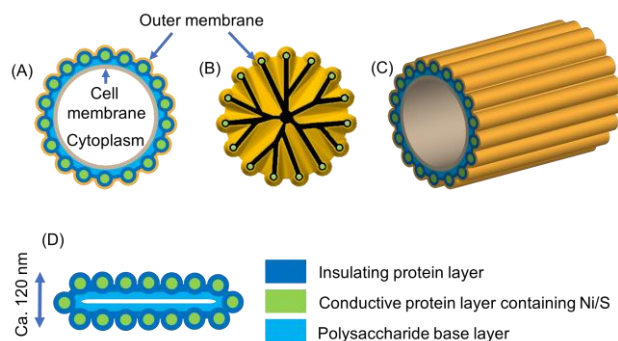


Figure 1. Schematic of a cable bacterium. Cross-section of a cable bacterium filament at the center of a cell (A) and at the junction (B) showing the cartwheel structure. 3D representation of the ridged cell (C). After the sequential extraction procedure, a flat ca. 120 nm thick fiber sheath is obtained, seen in (D). The spokes of the cartwheel are shown in black as its composition is unknown (adapted from Cornelissen et al.<sup>8</sup> and Boschker et al.<sup>11</sup>)

ToF-SIMS uses a polyatomic or gas cluster ion source in addition to monoatomic sources, and as such, it is less destructive as compared to NanoSIMS.  $\text{Bi}_3^+$  ion source was found to be both surface-sensitive as well as providing the best imaging contrast<sup>23</sup>. Large molecular fragments up to 1000 Da can be analyzed, and with a typical lateral resolution of 100 nm – 10  $\mu\text{m}$ <sup>24</sup>. Generally, two different modes are employed in ToF-SIMS<sup>25</sup>. The first one is the high current bunched (HCB) mode, also referred to as mass-spectrometry mode, which targets high mass resolution but has a restricted 2-10  $\mu\text{m}$  lateral resolution<sup>25,26</sup>. Mass resolution can be defined as the ability to distinguish two peaks of slightly different mass-to-charge ratios ( $m/\Delta m$ ) in a mass spectrum. HCB mode uses three electrostatic lenses and a primary ion buncher system, ensuring short pulses of less than one ns. Such short pulse duration results in a typically high mass resolution  $m/\Delta m > 10,000$ . The second ToF-SIMS mode is the burst alignment mode or fast-imaging (FI) mode, where a high lateral resolution of about 400 nm is obtained but with a loss of mass resolution<sup>27</sup>. A narrow beam is used in FI mode, with a beam diameter well below one micron using two electrostatic lenses. The time width of the primary ion pulse is in the order of tens of nanoseconds, leading to a low unit mass resolution ( $m/\Delta m \sim 200$ )<sup>25-27</sup>. Mass resolution can be improved by maintaining the lateral resolution of FI mode using delayed extraction. This third ToF-SIMS mode is termed as fast imaging delayed extraction (FI-DE). In delayed extraction, ion extraction is decoupled from ion generation by switching off the extraction voltage for several nanoseconds after firing the primary ion pulse. A plume of ions is obtained just over the surface, a field-free emission of secondary particles. Due to this decoupling, the long primary ion pulse required to obtain a high lateral resolution does not affect the mass resolution<sup>25,27</sup>. The plume moves away from the surface before the extraction voltage is switched on, because of which the topographic effects are reduced, the number of secondary ions collected increased, and sharper lateral images with a better signal are obtained. Quite recently, Benettoni et al. were able to obtain a high lateral resolution of ~100 nm on a chessboard sample, with a mass resolution in the order of 5000. However, the lateral resolution was reduced to 222 nm on an algal biofilm<sup>28</sup>.

Recently, TOF-SIMS analysis combined with in-situ AFM has generated the first insights into the conductive network of cable bacteria<sup>11</sup> (see Figure 1D for a schematic representation of results). To this end, ToF-SIMS HCB analysis using  $\text{Bi}_3^+$  was combined with interlaced argon cluster sputtering and applied to fiber sheaths. This provided high-resolution depth profiles of both organic and inorganic constituents at low lateral resolution<sup>11</sup>. High surface counts were recorded for amino acid fragments, including aromatic amino acids in both positive and negative modes. Nickel and Sulphur signals showed subsurface peaks in the positive and negative mode, suggesting that the fiber's central core is protein-rich with Ni and S. After 150s of sputtering, signals from the oxygen-rich fragments, including carbohydrate specific ions

peaked while the signals from nitrogen-containing fragments levelled off. By combining results from other complementary characterization techniques, a structural model of the fiber sheath was made (Figure 1D): fibers are made of protein, lying on top of a polysaccharide-rich base layer, most likely consisting of peptidoglycan. The fiber itself is made of a Ni-rich protein core surrounded by a thin layer of Ni-deficient protein, which is termed as a fiber core/shell structure<sup>11</sup>. Although the HCB mode was instrumental in identifying various fragments with a high mass resolution, it comes with a sacrifice of lateral resolution that does not allow to separately study the composition of the fibers and the cartwheel structure at the junctions<sup>11</sup>. To provide more detail on the conductive fibers present in the fiber sheath, we employed and compared the three mentioned ToF-SIMS modes. The FI-DE mode, which balances lateral and mass resolution, in combination with in-situ AFM is expected to offer the unique benefit of a direct and more detailed depth calibration.

## EXPERIMENTAL SECTION

**Sample preparation.** Sediments containing cable bacteria were collected from a salt marsh creek bed. These sediments were sieved, homogenized, repacked in PVC core liner tubes (diameter 40 mm), and were subsequently placed in aerated, artificial seawater. These incubations are known to consistently develop thick, ca. 4  $\mu\text{m}$  diameter, cable bacterium filaments, which facilitates their isolation from the sediment and fiber sheath extraction.

To collect the cable bacterium filaments and extract the fiber sheaths, a small amount of sediment was placed on a microscope cover slip. Multiple 20  $\mu\text{L}$  droplets of Milli-Q water were placed near the sediments. Under a stereomicroscope, filaments were picked from the sediments using custom-made glass hooks made from Pasteur pipets. Filaments were cleaned and washed at least six times by transferring them between droplets. The cleaned intact filaments were subsequently incubated in a 20  $\mu\text{L}$  droplet of sodium dodecyl sulfate (SDS) for 10 minutes, followed by six MilliQ droplet washes. Filaments were further subjected to a 10-minute incubation in a 20  $\mu\text{L}$  of 1mM sodium ethylenediaminetetraacetate (EDTA) solution, again followed by six washes in Milli-Q<sup>8</sup>. The extracted material represents the fiber sheath containing the conductive fibers.

Fiber sheaths were deposited as clumps on a 1 cm x 1 cm diced Au covered Si wafer for ToF-SIMS analysis. Samples were first imaged in an optical microscope to identify areas to be analyzed. Three samples prepared on different occasions were analyzed under HCB and FI-DE mode, and five areas from two clumps of fiber sheaths prepared during the same run were analyzed under combined ToF-SIMS/AFM mode.

For conductive AFM, one filament was deposited on a 1 cm x 1 cm diced  $\text{SiO}_2$  covered Si wafer (Figure S6). This wafer was then affixed onto a steel disc using silver paste (EM-Tec AG44 conductive silver paint). The detailed procedure can be found elsewhere<sup>10</sup>. Four replicates were analyzed using C-AFM.

**ToF-SIMS analysis.** ToF-SIMS analysis was performed using TOF.SIMS NCS (IONTOF GmbH, Germany) located at imec, Leuven (Belgium). For HCB mode, ToF-SIMS was carried out in interlaced mode using  $\text{Bi}_3^+$  analysis beam (30keV, current ~0.35 pA, 100x100  $\mu\text{m}^2$  area, 256x256 pixels) and  $\text{Ar}_{4000}^+$  gas cluster ion beam (Ar GCIB, 10keV, current 1nA, 400x400  $\mu\text{m}^2$  area). Fast imaging (FI) was done by finetuning the existing factory settings ( $\text{Bi}_3^+$ , 30 keV, ~0.12 pA, 30 x 30  $\mu\text{m}^2$ , 512 x 512 pixels). Only the surface scans were obtained in the case of FI mode. For FI-DE, the existing setting for fast imaging was initially set with  $\text{Bi}_3^+$  ions (30keV, current ~0.15pA, 30x30  $\mu\text{m}^2$  area). Parameters for delayed extraction were optimized, namely, delay time, the analyzer lens voltage, X/Y analyzer deflection plates, and surface and virtual drift potential (VDP)<sup>27</sup>. A delayed extraction of 85 ns was found to be appropriate. A cycle time of 50  $\mu\text{s}$  was used. In both cases, filaments were not necessarily sputtered until only the substrate remained, as shown in Figure 4.

SurfaceLab software (v7, IONTOF, Germany) was used for data analysis. In HCB mode, mass spectra were internally calibrated using

$C_2H_3^+$ ,  $C_3H_4^+$ ,  $C_3H_5^+$ ,  $C_4H_5^+$  and  $Au^+$ . Mass peaks were identified based on earlier ToF-SIMS work with cable bacteria<sup>11</sup>. In FI-DE mode, mass spectra were internally calibrated using  $C_2H_3^+$ ,  $C_3H_4^+$ ,  $C_3H_5^+$ , and  $C_4H_5^+$ . When necessary, lateral shift correction was done by using the *Shift correction* sub-program of the *Images* program. Regions of interest (ROIs) were created to analyze cell bodies and junctions separately (Figure 4). The peak list obtained from HCB mode was truncated to remove non-resolvable signals. Identified peaks from both HCB and FI-DE modes are provided in Tables S2 to S6.

Principal component analysis (PCA) was performed using OriginLab Pro v2020's principal component analysis app. Three replicates of profiles of various fragments from HCB and FI-DE modes were separately analyzed after mass calibration with the same peak lists. The peak width of each signal was adjusted by overlapping the three spectra and fixing the peak width. Depth (or analysis time) profiles of selected peaks were imported into OriginLab Pro software, in which the profiles of individual fragments were normalized to their maximum value. Profile data of the various masses until the maxima of the oxygen-containing organic ions were used for PCA, identical to those of Boschker et al.<sup>11</sup>. Fragments used in PCA are indicated in Tables S2 to S6.

**Combined ToF-SIMS/AFM analysis.** In-situ AFM was used in contact mode to analyze the depth at which the Ni signal maximum was found and to estimate the midpoint of the carbohydrate layer. PPP-EFM probes with a nominal spring constant of 3 N/m were used in contact mode. The AFM probe and the area to analyze were first aligned using a test area close to the area of interest. After ToF-SIMS obtained a scan of a known area, the coordinates were noted down by the Surfacelab software. Then, the sample was driven to the AFM part of the instrument. The area of interest was retrieved in the AFM by trial and error, and the Surfacelab software noted the coordinates of this area. The software calculates the lateral vector shift based on the two coordinates.

A  $10 \times 20 \mu\text{m}^2$  AFM image of the area to be sputtered was captured with a pixel size of about 78 nm. An enlarged area of about  $15 \times 30 \mu\text{m}^2$  was sputtered by  $Bi^{3+}$  ions with the conditions mentioned earlier. Sputtering was paused before and after the peak in  $Ni^+$  ion signal emerged. During the pause, the stage was moved within the same hybrid ToF-SIMS/AFM instrumental setup - without exposure to the lab atmosphere and therefore no contamination - to the in-situ AFM location. AFM imaging was taken from the sputtered area. These two images were leveled by mean plane subtraction, aligned using the "mutual crop" module of the *Gwyddion* software, and then the second image was subtracted from the first. In this difference image, the amount of material removed from the cell body can be determined. Another AFM image was taken at a point in the carbohydrate region.

**Conductive AFM.** AFM analysis was done on a Multimode 8 (Bruker, Santa Clara, CA, USA) with Nanoscope V controller located at UHasselt. A CDT-NCLR probe with a nominal spring constant of 72 N/m was used. A fiber sheath was placed on a silicon substrate with a 100 nm thick  $SiO_2$  layer acting as an insulator. This substrate was then connected to a steel disc using silver paste (Figure S6). One end of the fiber sheath was electrically connected to the substrate holder, while the other end of the filament was left free. Bias is applied to the sample

via the sample holder, and the conductive probe is electrically connected to the TUNA application module, which contains a current amplifier. This application module is, in turn, connected to the AFM controller. Current can only flow if there is an electrical connection between the substrate holder and the AFM probe, thereby completing the electrical circuit. Measurement was initially carried out in Scanasyt mode to obtain topography. After an area of interest was localized, AFM was switched to C-AFM mode, which works in contact mode.

Due to the high spring constant of the cantilever, specific areas from a cell were relatively easily removed by scratching a given area continuously in contact mode with a high force (15  $\mu\text{N}$ ) to disrupt more than half of the electrical connections within a cell. This creates a trench that goes all the way to the substrate. However, a much lower force (2.2  $\mu\text{N}$ ) was applied to gently scrape bacteria's surface to visualize the electrical pathways, identical to our earlier work<sup>10</sup>.

## RESULTS AND DISCUSSION

**Comparison of lateral imaging and mass resolution.** To qualitatively appreciate the mass resolution and quantitatively measure mass resolution, fiber sheaths were imaged using three different ToF-SIMS modes. Figure 2 shows cable bacterium filaments from a single sample preparation imaged with HCB (A and B), FI (C and D), and FI-DE (E and F). This illustrates the capabilities of these modes in terms of lateral imaging resolution (upper panels: A, C, and E) and mass resolution of ionized fragments (bottom panels: B, D, and F).

The HCB mode provides a high mass resolution spectrum (Figure 2A, B, S1). A high mass resolution of  $Ni^+$  ( $m/z = 57.93$ ) of 7,000 was measured. Figure 2A clearly shows the poor lateral imaging resolution, in which the filaments appear fuzzy and much thicker than their nominal width of 4 to 5  $\mu\text{m}$ . Using FI-mode led to a substantial improvement in lateral imaging resolution, with the cell junctions being resolved from the cell bodies (Figure 2C). However, the mass resolution was at best in the order of a few hundreds. For instance, the  $Ni^+$  signal was not resolved, because the low mass resolution (131), it also encompassed signals from  $C_2H_4NO^+$  ( $m/z = 58.029$ ) and  $C_3H_8N^+$  ( $m/z = 58.065$ ) (Figure 2C, D). This lack of mass resolution is insufficient for biological analysis.

In FI-DE mode, lateral resolution was sufficient to separate cell junctions from cell areas (Figure 2E), and the mass resolution of  $Ni^+$  was 2100 (Figure 2F). Complete spectra obtained from FI-DE can be seen in figure S1. Although the mass resolution does not match up to HCB, it was sufficient to resolve the  $Ni^+$  signal. FI-DE improved the lateral resolution, where the cell junctions and bodies are resolved. The mass resolution was found to be sufficient to resolve Ni and fragments of amino acids, polysaccharides, and others (see tables S2 – S6).

**Comparison of depth resolution.** We compared the depth resolution between HCB and FI-DE. HCB uses a dual-beam, where Argon GCIB is used to sputter away the analyzed area. However, FI-DE is a single beam measurement where  $Bi_3^+$  beam is also responsible for sputtering. Here we show that FI-DE has a better depth resolution compared to HCB.

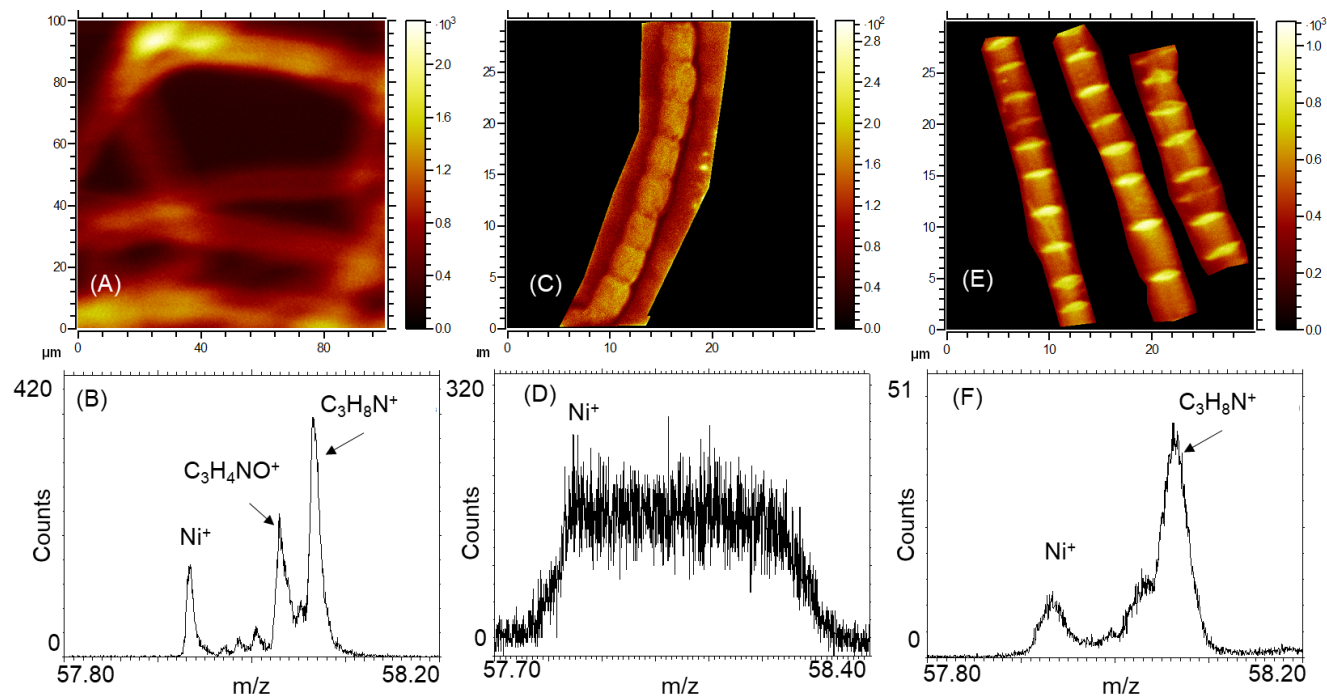


Figure 2. Study of ToF-SIMS imaging modes on the lateral and mass resolution: HCB (A and B), FI-DE (C and D) and FI mode (E and F). (A), (B) and (C) are the total intensity images. The lateral resolution of FI-DE (E) and FI (C) is better than HCB (A). On the other hand, the mass resolution ( $m/\Delta m$ ) of  $\text{Ni}^+$  of HCB mode (B) was 7000, whereas in FI-DE mode (D) was lower at 2100, sufficient to resolve  $\text{Ni}^+$  signal. Mass resolution in FI mode is insufficient to resolve  $\text{Ni}^+$ .

Figure S2 shows the normalized three main trends in the sputtering-time depth profiles as found in HCB mode, based on the study by Boschker et al.<sup>11</sup>. The first one or two data points are usually related to surface transients, i.e., C- or N-based ions derived from contamination (this surficial zone extends until the local minimum of  $\text{CHO}^+$  signal). Below this, the first signal observed are high levels of nitrogen-containing fragments such as  $\text{C}_4\text{H}_8\text{N}^+$ , a fragment of proline, an amino acid used in the synthesis of proteins, that stands for the profile of all amino acid fragments. Ni and its isotopes show a subsequent peak, and a third and broader peak is displayed by oxygen-containing fragments such as  $\text{CHO}^+$ , most likely derived from carbohydrates in the peptidoglycan layer. The  $\text{C}_4\text{H}_8\text{N}^+$  shows a very high surface signal, indicating the presence of protein layer at the surface. The sub-surface peak in Ni has been linked to a Ni-containing protein that likely plays a role in the electron transport within the conductive fibers<sup>11</sup>. As the intensity of  $\text{Ni}^+$  decreases, oxygen-containing fragments such as  $\text{CHO}^+$  becomes higher in intensity. A second Ni peak is seen at about 164s of sputtering time. Although not entirely resolved, this second peak is likely due to the Ni-protein layer in the bottom part of the fiber sheath, which is essentially a mirrored duplicate of the part of the sheath away from the substrate.

Principal component analysis (PCA) of selected peaks (Figure S3A, C) showed clustering of oxygen-containing fragments and nitrogen-containing fragments with Ni. Boschker et al. proposed that the fiber sheath is made of a thin protein layer containing Ni-containing proteins and a polysaccharide-rich layer present under the protein layer<sup>11</sup>. However, in many cases, depth smearing occurs due to a possible different structure (cell bodies vs. junction). When cells retain an amount of cytoplasm after incomplete extraction, only the first subsurface Ni peak can be detected<sup>11</sup>. So an additional benefit of FI-DE as employed here is that it also enables the imaging of the bottom part of the fiber sheath.

A significant improvement made with FI-DE is that regions of interest (ROIs) can be separately defined for the cell body and the cell junction (Figure 3A-C). Signals from the body of cable bacteria this can be studied separately from the cell junctions, which reduces depth smearing, as junctions are thicker than the rest of the filament<sup>8</sup>. Cell junctions can be distinguished from the rest of the bacteria in FI-DE by the total counts measured at the junction, possibly due to the higher material

yield. Cell junctions contain more material than the cell body, which implies more counts from this region (Figure 3A). Newly forming division planes, which are rings consisting of protein FtsZ<sup>29</sup> were not considered in the junctions analysis since it is not known whether their structure is similar to that of an established division plane. Depth resolution was further improved in FI-DE imaging since more data points were obtained for a given thickness of material sputtered thanks to a single beam. The first seven data points, corresponding to the local minimum in  $\text{CHO}^+$  signal, are again related to the surface transient, i.e., organic contamination on the surface.

The filament signals in FI-DE mode consistently revealed a sharp sub-surface Ni peak and a distinctive second peak (Figure 3D).  $\text{C}_4\text{H}_8\text{N}^+$  has an intense surface signal seen earlier in HCB mode and a secondary peak just before Ni signal reaches a peak, which was not seen in HCB mode. The carbohydrate oxygen-containing fragment  $\text{CHO}^+$  is prominently present between the two peaks of  $\text{Ni}^+$  signals and nitrogen-containing signals. The second peak of Ni signal and the peak of  $\text{C}_4\text{H}_8\text{N}^+$  signal confirm that Ni is found in the protein, and the basal sheath is held together by a carbohydrate-containing layer. The second  $\text{Ni}^+$  peak and  $\text{C}_4\text{H}_8\text{N}^+$  peak from the cell bodies (Figure 3E) were sharper than the signals from the filaments. This is because junctions are thicker and possibly have a different composition due to the presence of the cart-wheel structure. PCA analysis of the various identified fragments from cell bodies (Figure S3 B, D) showed a clustering of the nitrogen-containing fragments and the oxygen-containing fragments, similar to that seen in HCB mode.

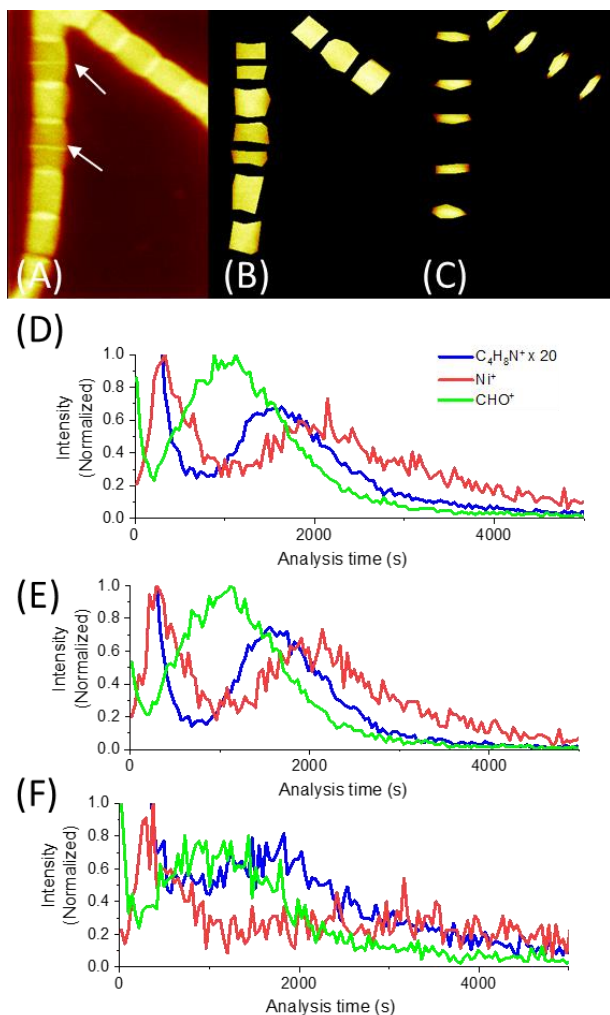


Figure 3. (A) Lateral total intensity image of two cable bacteria filaments, with two white arrows showing the newly forming cell junctions. The enhanced lateral resolution of FI-DE enabled the study of signals from various fragments from the body (B) and the junctions (C) separately. Trends of  $C_4H_8N^+$ ,  $Ni^+$ , and  $CHO^+$  signals, normalized to

their highest intensity, from the filaments (D), cell bodies (E), and cell junctions (F).  $C_4H_8N^+$  signal was magnified by 20x in order to show the second peak in the profile.

**Combined ToF-SIMS/AFM study of fiber sheaths.** Depth profiles in ToF-SIMS provide the intensity of various fragments as a function of time. By using in-situ AFM at appropriate intervals, analysis time can be translated in terms of distance. Depth patterns of various fragments as obtained by combining AFM and HCB mode were previously shown by Boschker et al.<sup>11</sup>. Here we combine AFM with FI-DE mode. Figure 4 describes how the distance of the  $Ni^+$  signal from the top surface is measured. Figure 4A is the height image before analysis commenced. The change of normalized intensity of the sum of two Ni isotopes,  $^{58}Ni^+$  and  $^{60}Ni^+$  and  $CHO^+$  signals during sputtering are given as a function of data points (Figure 4F). One data point corresponds to one scan by the  $Bi^{3+}$  ions of the given area. Profiles of  $^{58}Ni^+$  and  $^{60}Ni^+$  and  $CHO^+$  fragments in Figure 4F were obtained from the dotted blue polygons in Figure 4D. As the combined Ni signal went higher in intensity, the analysis was paused at datapoint 6, and another AFM image was taken (Figure 4B).

Subtracting Figure 4B from 4A gave a difference image, Figure 4C. Sputtered depth was measured by averaging the area within the dotted blue polygons of Figure 4C and subtracting from the substrate's height. This corresponds to  $9.1 \pm 7.7$  nm. Another AFM image was taken at data point 10 after the peak of  $Ni^+$  signal was crossed. A third AFM image was taken at datapoint 25, in the carbohydrate-rich region. After measuring the sputtered depths for data points 10 and 25, a line fit was made. The initial condition was that no material is removed before the commencement of analysis (i.e.,  $y(x=0) = 0$  nm). The peak of  $Ni^+$  signal was seen at datapoint 7, corresponding to 12.7 nm. Based on an average of five replicates, an average depth of  $11.8 \pm 0.6$  nm was measured for the Ni maximum, slightly lower than the previously reported value of  $15 \pm 3$  nm<sup>11</sup>. However, the midpoint of the flat region of the oxygen-containing organics varied between samples (between 32 nm and 68 nm, see table S1). This is probably because different filaments containing varied amount of cytoplasm, although undergoing the same extraction procedure.

By combining in-situ AFM measurements with ToF-SIMS, we measured the depth of  $Ni^+$  without having to remove the sample out of vacuum. This is of importance to materials that are sensitive to exposure to atmospheric exposure. Also, keeping the sample within the equipment ensures the same instrument parameters such as vacuum and analysis beam conditions before and after AFM measurements. Lateral resolution obtained by FI-DE ensured a good correlation between SIMS and AFM data, and a more accurate determination of the depth at which Ni signals reached a peak in its counts.

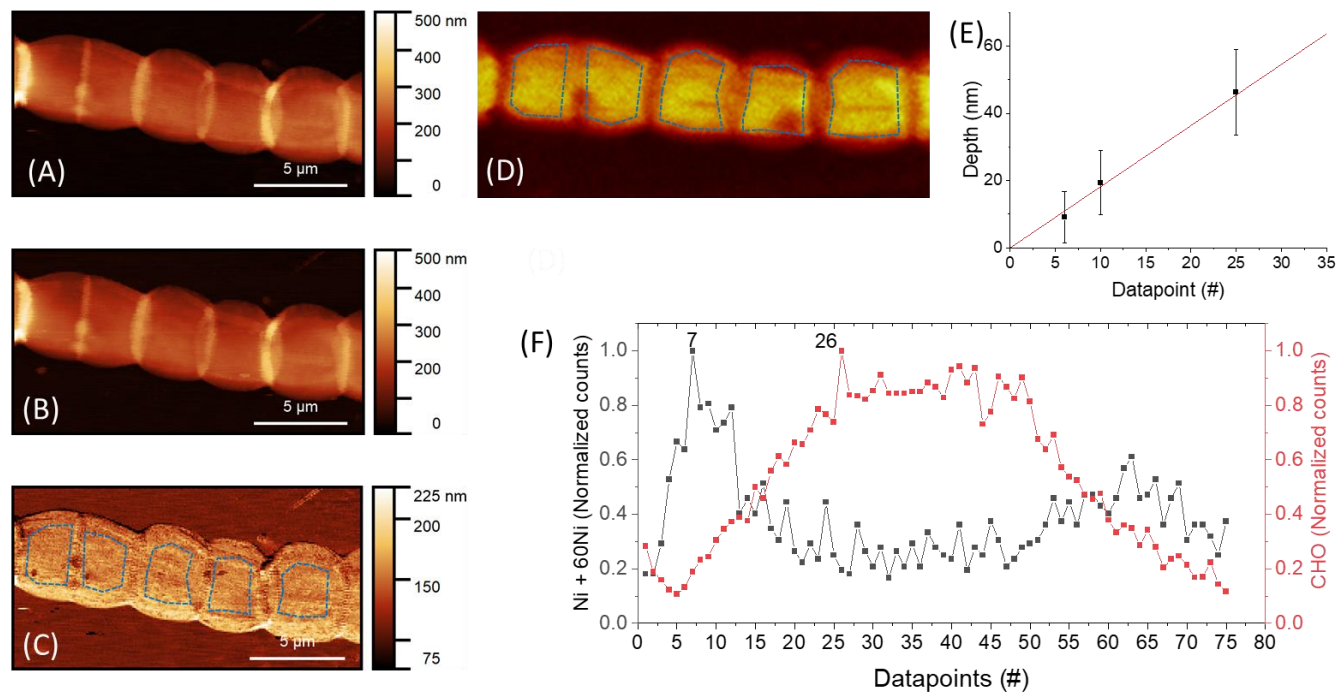


Figure 4. Combined ToF-SIMS/AFM analysis of a fiber sheath filament. An AFM image was captured (A) before sputtering and (B) after sputtering until datapoint 6. The total intensity ToF-SIMS image is shown in (D). (B) and (A) were aligned, and (B) was subtracted from (A), resulting in a difference image (C). Removed thickness was calculated by subtracting the substrate's mean height from the mean height of the bacteria body (dotted blue polygons), plotted in (E). (F) shows the change of Ni+ and CHO+ counts (normalized, obtained from cell bodies, marked as dotted blue polygons in D) as a function of captured data points. Ni+ peak is seen at datapoint 7, and CHO+ signal reaches a maximum at datapoint 26. The second Ni peak is seen at datapoint 64.

**Composition of the cell junctions.** Cell junctions contain the interconnecting structures that provide cable bacteria filaments with a redundant failsafe electrical network<sup>10</sup>. The cartwheel structure present at the junctions is suspected of containing the interconnecting structure, although there is no direct proof available<sup>8,10</sup>. Interestingly, junctions in fiber sheaths appear flatter compared to intact filaments<sup>8</sup>. Thanks to the lateral resolution offered by FI-DE, we can isolate signals from the junctions. Due to the improved depth resolution, we were able to study the various profiles' trends as a function of depth.

Profiles of the various fragments from the junctions showed similar trends (Figure 3F). Ni signal showed a subsurface peak, which comes from the conductive fibers that run parallel along with the cells and across the junction (Figure 3F, S4B). The amino acid peak is not as pronounced as that seen in the cell body. It appears that there are relatively more amino acid fragments between the two sheaths at the junction as compared to the cell body (Figure S4A). Also, the rate of a decreased intensity of the second amino acid peak from the cell junctions is lower. A look at the total number of signals of the various identified protein and carbohydrate fragments, normalized to the total counts of identified fragments, indicates that Ni's ratio to protein fragments at the junction is lower than that of the body (Figure S5). The relative amount of Ni present in the junction is identical to that of the body, suggesting that Ni is absent within the junction. Hence, the junction's interconnects are either damaged; its composition is different from the fibers, or both. However, the LEXRF analysis of fiber sheath<sup>11</sup> indicates a higher amount of Ni in certain sections of the sheath. Additional studies are required, such as analysis of cross-sections to arrive at a definite conclusion.

A conductive AFM experiment was carried out on a fiber sheath by intentionally disrupting the conductive pathways identical to those performed on untreated intact filaments<sup>10</sup> (Figure S6), to check whether the electrical interconnections seen in the latter are present in the former. The anti-parallel cuts in the filaments can be seen as trenches in the height image, also marked by green arrows (Figure 5). Carbon paste, connected to the fiber sheath away from the top-left corner (not seen), acts as an electrode. The AFM probe acts as the second electrode.

A pixel will appear bright in the AFM current image (figure 5B) if the AFM probe that is positioned on the fiber sheath at that pixel is electrically connected to both the electrodes. Conductive areas can be seen from the top-left until the first cut. Some areas that still remain electrically connected to the carbon paste can be seen between the first cut and the second, along the left edge. The rest of the area remains non-conductive, as they are not electrically connected to the carbon paste. This shows that the junction in the extracted fiber sheaths does not provide electrical interconnection of fibers, as seen in untreated filaments<sup>10</sup>. As already hypothesized from the FI-DE experiments, C-AFM measurements suggest that interconnects within the junction of extracted fiber sheaths are either damaged, or its composition is different from the fibers, or both. Further research is needed to resolve this issue and elucidate the cartwheel structure's nature in the junction of cable bacteria.

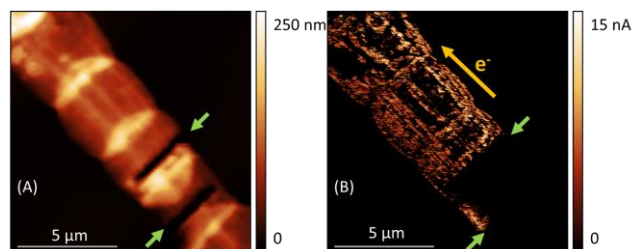


Figure 5. Conductive AFM images (A) Topography map and (B) Current map of a fiber sheath with two anti-parallel cuts across its width (green arrows). The fiber sheath is biased using carbon paste on the top-left corner (not seen). As the probe scans the surface from the bottom, structures electrically connected between the area under the AFM probe and the carbon paste appear bright, i.e. conductive, seen in (B). The direction of current flow is given by the orange arrow in (B).

## CONCLUSION

We investigated the structure and composition of cable bacteria with an enhanced lateral resolution, allowing differentiation between the cell body and the structured cartwheel junctions. The combination of ToF-SIMS FI-DE and in-situ AFM proved to be a powerful approach for this. Three ToF-SIMS modes were compared, viz., high current bunched (HCB), fast imaging (FI), and fast imaging delayed extraction (FI-DE). HCB provided the best mass resolution but lacked lateral resolution. On the other hand, FI mode provided a high lateral resolution but lacked mass resolution, which at best was in the order of a few hundreds. However, we found that FI-DE provide a good balance between mass and lateral imaging resolution. Not only a sub-micron resolution was obtained, but we observed the mass resolution to be sufficient to resolve signals such as Ni and other protein and carbohydrate related fragments. In order to avoid depth smearing, we used ROIs to analyze the bodies and junctions of the filaments separately, thanks to an improved lateral resolution. Ni signals reached a subsurface peak, followed by a decrease, and then reached a second maximum. The secondary Ni peak was not earlier seen with HCB analysis.

The maximum intensity of CHO<sup>+</sup> signal was found between the two Ni maxima, indicating a carbohydrate-rich material. Furthermore, we also observed enhanced depth resolution by following the depth profile of C<sub>4</sub>H<sub>8</sub>N<sup>+</sup> signal, in which we observed a secondary peak just before the second maxima of the Ni<sup>+</sup> signal. This confirms the earlier result that Ni is present in the still-unidentified protein. By using an advantageous combination of ToF-SIMS and AFM, we were able to carry out both SIMS and AFM imaging in an ultra-high vacuum, avoiding contamination by bringing the sample to atmospheric conditions for external AFM imaging. Not only finding the sputtered location in an external AFM would have been difficult and time-consuming, to analyze the same area back in SIMS with the right orientation would be daunting. We were able to determine the depth of subsurface maxima of Ni<sup>+</sup> signal and the various depths at which carbohydrate signals were found. Comparing Ni to protein ratio in body and junction of bacteria indicated a higher ratio at the body than the junction. Also, Ni's relative counts at the body were equal to that of the junctions, indicating Ni's absence within the junction. This absence could be attributed to the junction and body composition differences or the interconnecting structure between adjacent cells seen in intact filaments is damaged during the extraction procedure or both. C-AFM measurements show that the interconnections at the junction seen earlier in intact filaments are not present in the fiber sheath. Not much is yet known about the composition and properties of the cartwheel structure in intact filaments. Cross-sections of intact filaments and fiber sheaths obtained by cryo-microtome and the study of these cross-sections using ToF-SIMS and other complementary techniques such as C-AFM could give better insight into the composition of the cell-cell junction. Furthermore, the continued use of the proposed ToF-SIMS/SPM measurement methodology together with complementary analytical and electrical techniques, could be powerful towards a better understanding of the underlying electrical transport properties in cable bacteria and in particular to clarify the role of Ni and S. This teaming up with complementary techniques is essential since ToF-SIMS can provide insights on the chemical composition of cable bacteria, but is not a quantitative technique and therefore does not allow to quantify Ni and S density. In our recent work on the intrinsic electrical properties of cable bacteria, we have observed an Arrhenius-type relation for the temperature dependence of the electrical conductivity and electron mobility over a broad temperature range (-195°C to +50°C), demonstrating that charge transport is thermally activated<sup>30</sup>.

From a more general analytical perspective, the proposed methodology of ToF-SIMS in FI-DE-mode, combined with AFM, could also be beneficial in resolving the structure and composition of other biological systems. An in-situ AFM can be used to measure depth of various features of interest. However, an AFM is foremost an imaging (microscopy) tool. Hence, an AFM can also be used to identify area of interest. For example, when micron-sized cells are dispersed over a substrate, it is impossible to see them using the in-built camera of the ToF-SIMS equipment. The in-situ AFM can be used to image areas to identify the location of these cells in a given area in the substrate before they are analysed using SIMS, thus saving time.

## ASSOCIATED CONTENT

### Supporting Information

The Supporting Information is available free of charge on the ACS Publications website.

HCB and FI-DE ToF-SIMS spectra of fiber sheath, trends of various fragments as a function of sputter time, PCA analysis of fiber sheath spectra in HCB and FI-DE modes, comparison of three typical trends at the body and junction, comparison of various fragments normalized to total intensity of identified fragments, schematic of C-AFM setup, depth measurements of Ni<sup>+</sup> and CHO<sup>+</sup> signals, lists of identified fragments associated with protein layer, Ni, polysaccharide layer, other general fiber sheath fragments, and fragments derived from medium, wafer and sediment matrix. ( PDF)

## AUTHOR INFORMATION

### Corresponding Author

\*jean.manca@uhasselt.be

### Author Contributions

The manuscript was written through contributions of all authors. All authors have given approval to the final version of the manuscript

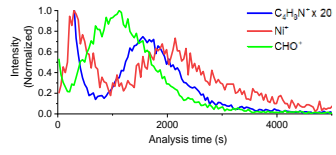
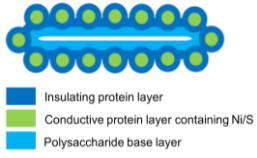
## ACKNOWLEDGMENT

The authors acknowledge Bart Cleuren and Robin Bonné for the discussion on the C-AFM experiment. The authors acknowledge the grants given by the Research Foundation – Flanders (FWO) (G031416N to RTE, JM and FJRM; G038819N to FJRM) and the Netherlands Organization for Scientific Research (NWO) (VICI grant 016.VICI.170.072 awarded to FJRM). ToF-SIMS analysis was rendered possible thanks to the grant awarded to imec vzw and Hasselt University by the Hercules foundation (now FWO; grant no. ZW/13/07 awarded to JM and AF).

## REFERENCES

- (1) Pfeffer, C.; Larsen, S.; Song, J.; Dong, M.; Besenbacher, F.; Meyer, R. L.; Kjeldsen, K. U.; Schreiber, L.; Gorby, Y. A.; El-Naggar, M. Y.; Leung, K. M.; Schramm, A.; Risgaard-Petersen, N.; Nielsen, L. P. Filamentous Bacteria Transport Electrons over Centimetre Distances. *Nature* **2012**, *491* (7423), 218–221. <https://doi.org/10.1038/nature11586>.
- (2) Schauer, R.; Risgaard-Petersen, N.; Kjeldsen, K. U.; Bjerg, J. J. T.; Jorgensen, B. B.; Schramm, A.; Nielsen, L. P. Succession of Cable Bacteria and Electric Currents in Marine Sediment. *ISME J.* **2014**, *8* (6), 1314–1322. <https://doi.org/10.1038/ismej.2013.239>.
- (3) Meysman, F. J. R. Cable Bacteria Take a New Breath Using Long-Distance Electricity. *Trends Microbiol.* **2018**, *26* (5), 411–422. <https://doi.org/10.1016/j.tim.2017.10.011>.
- (4) Risgaard-Petersen, N.; Kristiansen, M.; Frederiksen, R. B.; Dittmer, A. L.; Bjerg, J. T.; Trojan, D.; Schreiber, L.; Damgaard, L. R.; Schramm, A.; Nielsen, L. P. Cable Bacteria in Freshwater Sediments. *Appl. Environ. Microbiol.* **2015**, *81* (17), 6003–6011. <https://doi.org/10.1128/AEM.01064-15>.
- (5) Müller, H.; Bosch, J.; Griebler, C.; Damgaard, L. R.; Nielsen, L. P.; Lueders, T.; Meckenstock, R. U. Long-Distance Electron Transfer by Cable Bacteria in Aquifer Sediments. *ISME J.* **2016**, *10* (8), 2010–2019. <https://doi.org/10.1038/ismej.2015.250>.
- (6) Malkin, S. Y.; Rao, A. M.; Seitaj, D.; Vasquez-Cardenas, D.; Zetsche, E.-M.; Hidalgo-Martinez, S.; Boschker, H. T.; Meysman, F. J. Natural Occurrence of Microbial Sulphur Oxidation by Long-Range Electron Transport in the Seafloor. *ISME J.* **2014**, *8* (9), 1843–1854. <https://doi.org/10.1038/ismej.2014.41>.

- (7) Burdorf, L. D. W.; Trammer, A.; Seitaj, D.; Meire, L.; Hidalgo-Martinez, S.; Zetsche, E. M.; Boschker, H. T. S.; Meysman, F. J. R. Long-Distance Electron Transport Occurs Globally in Marine Sediments. *Biogeosciences* **2017**, *14* (3), 683–701. <https://doi.org/10.5194/bg-14-683-2017>.
- (8) Cornelissen, R.; Bøggild, A.; Thiruvallur Eachambadi, R.; Koning, R. I.; Kremer, A.; Hidalgo-Martinez, S.; Zetsche, E.-M.; Damgaard, L. R.; Bonn , R.; Drijkoningen, J.; Geelhoed, J. S.; Boesen, T.; Boschker, H. T. S.; Valcke, R.; Nielsen, L. P.; D'Haen, J.; Manca, J. V.; Meysman, F. J. R. The Cell Envelope Structure of Cable Bacteria. *Front. Microbiol.* **2018**, *9*, 3044. <https://doi.org/10.3389/fmicb.2018.03044>.
- (9) Meysman, F. J. R.; Cornelissen, R.; Trashin, S.; Bonn , R.; Martinez, S. H.; van der Veen, J.; Blom, C. J.; Karman, C.; Hou, J. L.; Eachambadi, R. T.; Geelhoed, J. S.; Wael, K. De; Beaumont, H. J. E.; Cleuren, B.; Valcke, R.; van der Zant, H. S. J.; Boschker, H. T. S.; Manca, J. V. A Highly Conductive Fibre Network Enables Centimetre-Scale Electron Transport in Multicellular Cable Bacteria. *Nat. Commun.* **2019**, *10* (1). <https://doi.org/10.1038/s41467-019-12115-7>.
- (10) Thiruvallur Eachambadi, R.; Bonn , R.; Cornelissen, R.; Hidalgo-Martinez, S.; Vangronsveld, J.; Meysman, F. J. R.; Valcke, R.; Cleuren, B.; Manca, J. V. An Ordered and Fail-Safe Electrical Network in Cable Bacteria. *Adv. Biosyst.* **2020**, 2000006. <https://doi.org/10.1002/adbi.202000006>.
- (11) Boschker, H. T. S.; Cook, P. L.; Polerecky, L.; Thiruvallur Eachambadi, R.; Lozano, H.; Hidalgo-Martinez, S.; Khalek, D.; Spampinato, V.; Claes, N.; Kundu, P.; Wang, D.; Bals, S.; Cavezza, F.; Hauffman, T.; Tataru Bjerg, J.; Skirtach, A. G.; Kochan, K.; McKee, M.; Wood, B.; Bedolla, D.; Geerlings, N. M.; Van Gerven, N.; Remaut, H.; Millan-Solsona, R.; Fumagalli, L.; Nielsen, L.-P.; Franquet, A.; Manca, J. V.; Gomila, G.; Meysman, F. J. R. Efficient Long-Range Conduction in Cable Bacteria through Nickel Protein Wires. *bioRxiv* **2020**, 2020.10.23.351973. <https://doi.org/10.1101/2020.10.23.351973>.
- (12) Hanrieder, J.; Malmberg, P.; Ewing, A. G. Spatial Neuroproteomics Using Imaging Mass Spectrometry. *Biochimica et Biophysica Acta - Proteins and Proteomics*. Elsevier July 1, 2015, pp 718–731. <https://doi.org/10.1016/j.bbapap.2014.12.026>.
- (13) Jungnickel, H.; Laux, P.; Luch, A. Time-of-Flight Secondary Ion Mass Spectrometry (ToF-SIMS): A New Tool for the Analysis of Toxicological Effects on Single Cell Level. *Toxics* **2016**, *4* (1), 5. <https://doi.org/10.3390/toxics4010005>.
- (14) Spengler, B. Mass Spectrometry Imaging of Biomolecular Information. *Analytical Chemistry*. American Chemical Society January 6, 2015, pp 64–82. <https://doi.org/10.1021/ac504543v>.
- (15) Smart, K. E.; Smith, J. A. C.; Kilburn, M. R.; Martin, B. G. H.; Hawes, C.; Grovenor, C. R. M. High-Resolution Elemental Localization in Vacuolate Plant Cells by Nanoscale Secondary Ion Mass Spectrometry. *Plant J.* **2010**, *63* (5), 870–879. <https://doi.org/10.1111/j.1365-3113X.2010.04279.x>.
- (16) Malherbe, J.; Penen, F.; Isaure, M. P.; Frank, J.; Hause, G.; Dobritsch, D.; Gontier, E.; Horr ard, F.; Hillion, F.; Schauml ffel, D. A New Radio Frequency Plasma Oxygen Primary Ion Source on Nano Secondary Ion Mass Spectrometry for Improved Lateral Resolution and Detection of Electropositive Elements at Single Cell Level. *Anal. Chem.* **2016**, *88* (14), 7130–7136. <https://doi.org/10.1021/acs.analchem.6b01153>.
- (17) Ag -Gonzalez, P.; J hne, S.; Phan, N. T. N. SIMS Imaging in Neurobiology and Cell Biology. *Journal of Analytical Atomic Spectrometry*. Royal Society of Chemistry July 1, 2019, pp 1355–1368. <https://doi.org/10.1039/c9ja00118b>.
- (18) Nu ez, J.; Renslow, R.; Cliff, J. B.; Anderton, C. R. NanoSIMS for Biological Applications: Current Practices and Analyses. *Biointerphases* **2018**, *13* (3), 03B301. <https://doi.org/10.1116/1.4993628>.
- (19) Gyngard, F.; Steinhauser, M. L. Biological Explorations with Nanoscale Secondary Ion Mass Spectrometry. *Journal of Analytical Atomic Spectrometry*. Royal Society of Chemistry August 1, 2019, pp 1534–1545. <https://doi.org/10.1039/c9ja00171a>.
- (20) Georgantzopoulou, A.; Serchi, T.; Cambier, S.; Leclercq, C. C.; Renaut, J.; Shao, J.; Kruszewski, M.; Lentzen, E.; Grysan, P.; Esvara, S.; Audinot, J. N.; Contal, S.; Ziebel, J.; Guignard, C.; Hoffmann, L.; Murk, A. T. J.; Gutleb, A. C. Effects of Silver Nanoparticles and Ions on a Co-Culture Model for the Gastrointestinal Epithelium. *Part. Fibre Toxicol.* **2016**, *13* (1), 9. <https://doi.org/10.1186/s12989-016-0117-9>.
- (21) Lee, R. F. S.; Riedel, T.; Escrig, S.; MacLachlan, C.; Knott, G. W.; Davey, C. A.; Johnsson, K.; Meibom, A.; Dyson, P. J. Differences in Cisplatin Distribution in Sensitive and Resistant Ovarian Cancer Cells: A TEM/NanoSIMS Study. *Metallomics* **2017**, *9* (10), 1413–1420. <https://doi.org/10.1039/C7MT00153C>.
- (22) Geerlings, N. M. J.; Karman, C.; Trashin, S.; As, K. S.; Kienhuis, M. V. M.; Hidalgo-Martinez, S.; Vasquez-Cardenas, D.; Boschker, H. T. S.; de Wael, K.; Middelburg, J. J.; Polerecky, L.; Meysman, F. J. R. Division of Labor and Growth during Electrical Cooperation in Multicellular Cable Bacteria. *Proc. Natl. Acad. Sci. U. S. A.* **2020**, *117* (10), 5478–5485. <https://doi.org/10.1073/pnas.1916244117>.
- (23) Dubey, M.; Brison, J.; Grainger, D. W.; Castner, D. G. Comparison of Bi<sup>1+</sup>, Bi<sup>3+</sup> and C<sub>60</sub><sup>+</sup> Primary Ion Sources for ToF-SIMS Imaging of Patterned Protein Samples. *Surf. Interface Anal.* **2011**, *43* (1–2), 261–264. <https://doi.org/10.1002/sia.3537>.
- (24) Decelle, J.; Veronesi, G.; Gallet, B.; Stryhanyuk, H.; Benettoni, P.; Schmidt, M.; Tucoulou, R.; Passarelli, M.; Bohic, S.; Clode, P.; Musat, N. Subcellular Chemical Imaging: New Avenues in Cell Biology. *Trends in Cell Biology*. Elsevier Ltd March 1, 2020, pp 173–188. <https://doi.org/10.1016/j.tcb.2019.12.007>.
- (25) Vanbellinghen, Q. P.; Elie, N.; Eller, M. J.; Della-Negra, S.; Touboul, D.; Brunelle, A. Time-of-Flight Secondary Ion Mass Spectrometry Imaging of Biological Samples with Delayed Extraction for High Mass and High Spatial Resolutions. *Rapid Commun. Mass Spectrom.* **2015**, *29* (13), 1187–1195. <https://doi.org/10.1002/rcm.7210>.
- (26) Kubicek, M.; Holzlechner, G.; Opitz, A. K.; Larisegger, S.; Hutter, H.; Fleig, J. A Novel ToF-SIMS Operation Mode for Sub 100 Nm Lateral Resolution: Application and Performance. *Appl. Surf. Sci.* **2014**, *289* (100), 407–416. <https://doi.org/10.1016/j.apsusc.2013.10.177>.
- (27) Henss, A.; Otto, S.-K.; Schaepe, K.; Pauksch, L.; Lips, K. S.; Rohnke, M. High Resolution Imaging and 3D Analysis of Ag Nanoparticles in Cells with ToF-SIMS and Delayed Extraction. *Biointerphases* **2018**, *13* (3), 03B410. <https://doi.org/10.1116/1.5015957>.
- (28) Benettoni, P.; Stryhanyuk, H.; Wagner, S.; Kollmer, F.; Moreno Osorio, J. H.; Schmidt, M.; Reemtsma, T.; Richnow, H. H. Identification of Nanoparticles and Their Localization in Algal Biofilm by 3D-Imaging Secondary Ion Mass Spectrometry. *J. Anal. At. Spectrom.* **2019**, *34* (6), 1098–1108. <https://doi.org/10.1039/c8ja00439k>.
- (29) Jiang, Z.; Zhang, S.; Klausen, L. H.; Song, J.; Li, Q.; Wang, Z.; Stokke, B. T.; Huang, Y.; Besenbacher, F.; Nielsen, L. P.; Dong, M. In Vitro Single-Cell Dissection Revealing the Interior Structure of Cable Bacteria. *Proc. Natl. Acad. Sci.* **2018**, 201807562. <https://doi.org/10.1073/pnas.1807562115>.
- (30) Bonn , R.; Hou, J. L.; Hustings, J.; Wouters, K.; Meert, M.; Hidalgo-Martinez, S.; Cornelissen, R.; Morini, F.; Thijs, S.; Vangronsveld, J.; Valcke, R.; Cleuren, B.; Meysman, F. J. R.; Manca, J. V. Intrinsic Electrical Properties of Cable Bacteria Reveal an Arrhenius Temperature Dependence. *Sci. Rep.* **2020**, *10* (1), 1–8. <https://doi.org/10.1038/s41598-020-76671-5>.



## Supporting information

# Enhanced laterally resolved ToF-SIMS and AFM imaging of the electrically conductive structures in cable bacteria

Raghavendran Thiruvallur Eachambadi<sup>[a]</sup>, Henricus T. S. Boschker<sup>[b], [c]</sup>, Alexis Franquet<sup>[d]</sup>, Valentina Spampinato<sup>[d]</sup>, Silvia Hidalgo-Martinez<sup>[c]</sup>, Roland Valcke<sup>[e]</sup>, Filip J. R. Meysman<sup>[c], [b]</sup>, Jean V. Manca<sup>[a]</sup>

[a] UHasselt – X-LAB, Agoralaan, 3590 Diepenbeek, Belgium

[b] Department of Biotechnology, Delft University of Technology, Van der Maasweg 9, 2629 HZ Delft, The Netherlands

[c] Department of Biology, University of Antwerp, Universiteitsplein 1, 2610 Wilrijk, Belgium

[d] Materials and Components Analysis – Compositional Analysis, Imec vzw, Kapeldreef 75, 3001 Leuven, Belgium

[e] UHasselt – Molecular and Physical Plant Physiology, Agoralaan, 3590 Diepenbeek, Belgium

## Table of contents

Figure S1: Spectra obtained from (left) HCB imaging and (right) FI-DE of fiber sheath	S2
Figure S2: Trends of selected fragments as a function of sputter time in HCB mode	S3
Figure S3: Principal component analysis of fiber sheath spectra obtained from HCB and FI-DE modes	S4
Figure S4: Comparison of three typical trends at the body and junction	S5
Figure S5: Comparison of protein-related, carbohydrate-related fragments and Ni at the body and junction	S6
Figure S6: Schematic of conductive AFM setup	S6
Table S1: Depth measurements of Ni <sup>+</sup> signal, CHO <sup>+</sup> signal and thickness of filament measured at the center of cell body	S7
Table S2: Fragments associated with protein layer	S7
Table S3: Ni signal	S8
Table S4: Fragments associated with polysaccharide layer	S8
Table S5: Other general fiber sheath fragments	S9
Table S6: Fragments likely derived from medium, wafer and sediment matrix	S10

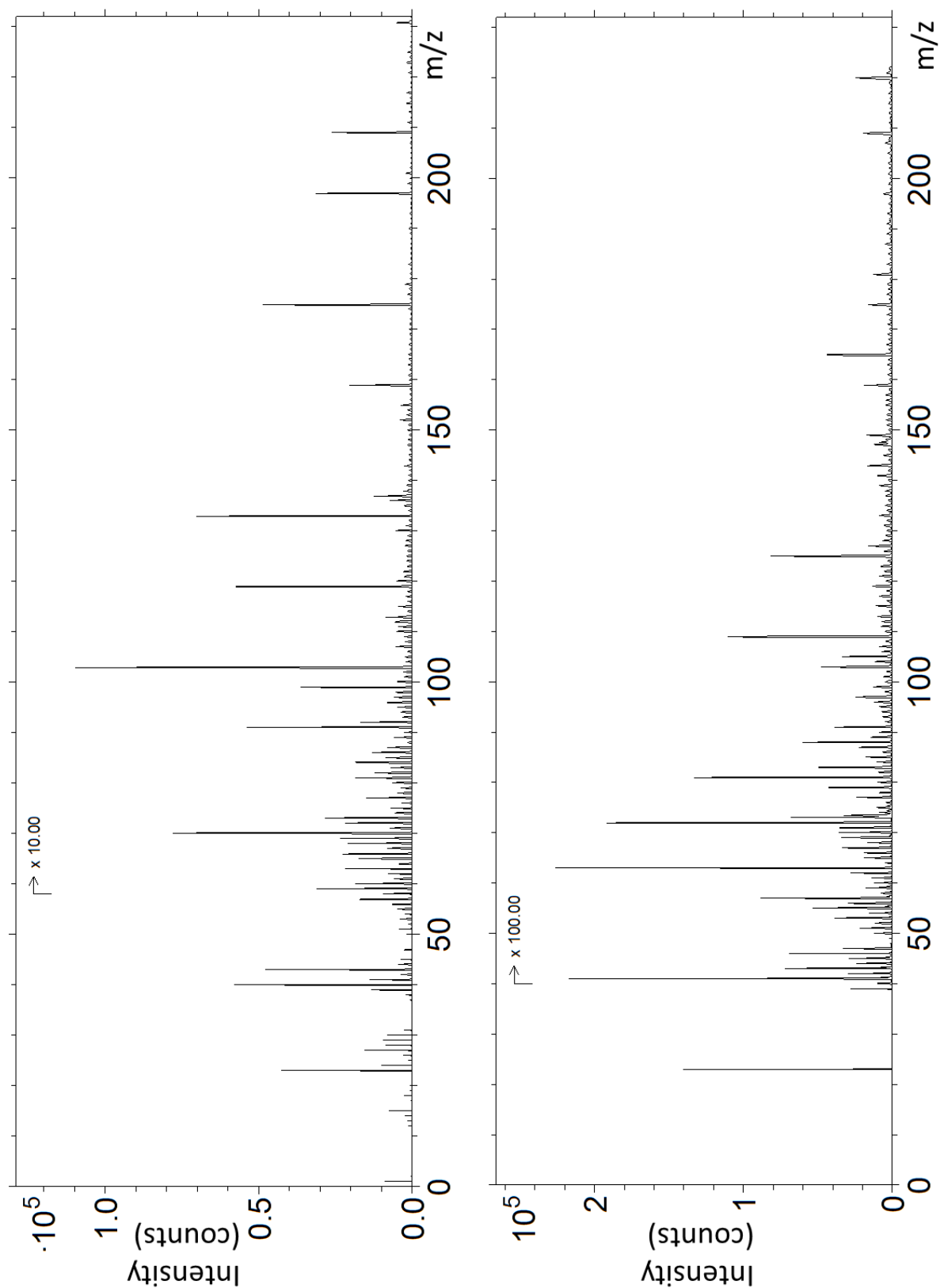


Figure S1: Spectra obtained from (left) HCB imaging and (right) FI-DE of fiber sheath.

The m/z range of HCB spectrum was chosen to reflect the available m/z range of FI DE mode due to the cycle time of 50  $\mu$ s of the latter.

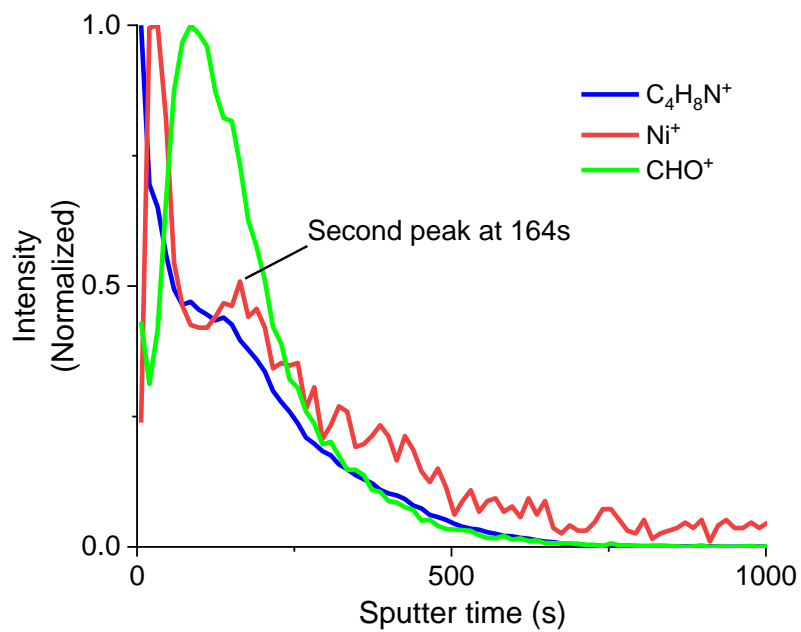


Figure S2. Trends of selected fragments as a function of sputter time in HCB mode. The first two datapoints are related to surface transient. The second peak of Ni<sup>+</sup> is seen after 164 seconds of sputtering.

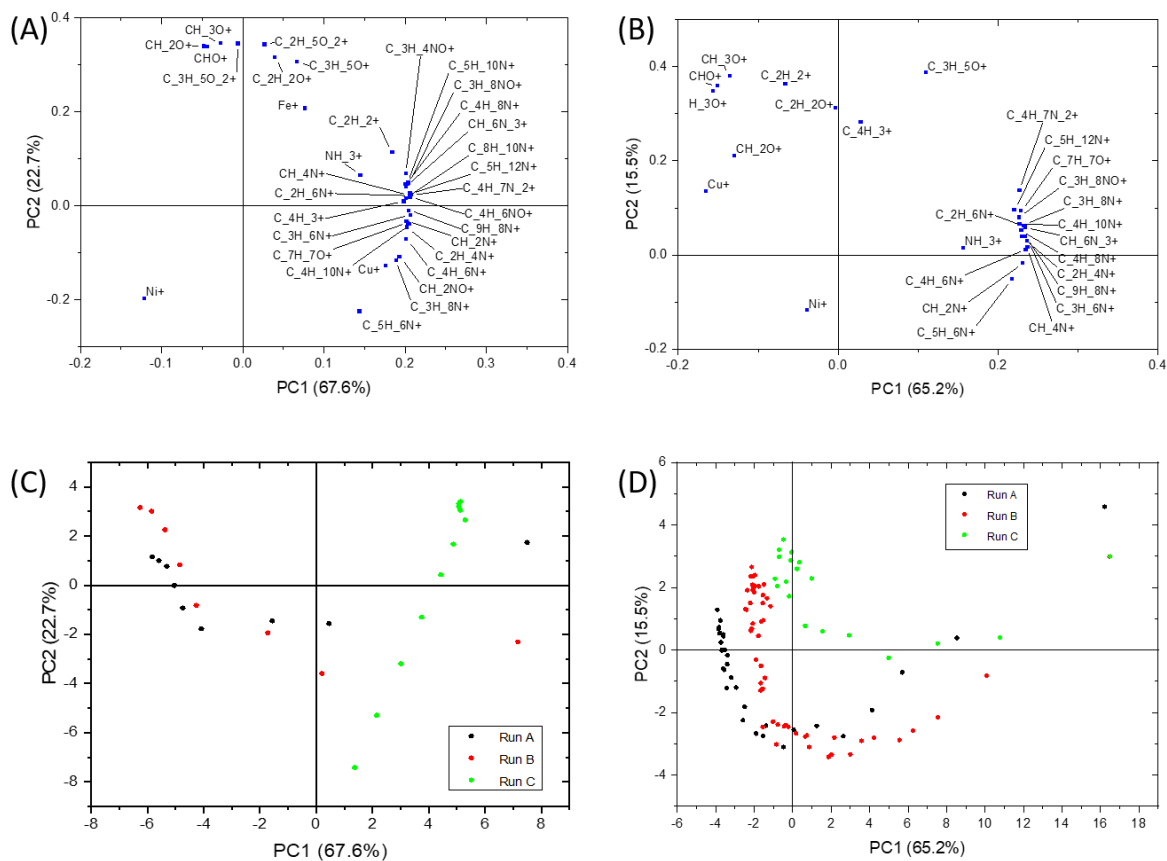


Figure S3: Principal component analysis of fiber sheath spectra obtained from HCB and FI-DE modes.

PCA of HCB mode (A, C) and FI-DE (B, D) were obtained from three datasets each. Signals of fragments until the maximum of carbohydrate-related signals were used in PCA analysis. Amino acid fragments cluster together as are the oxygen containing carbohydrate fragments.

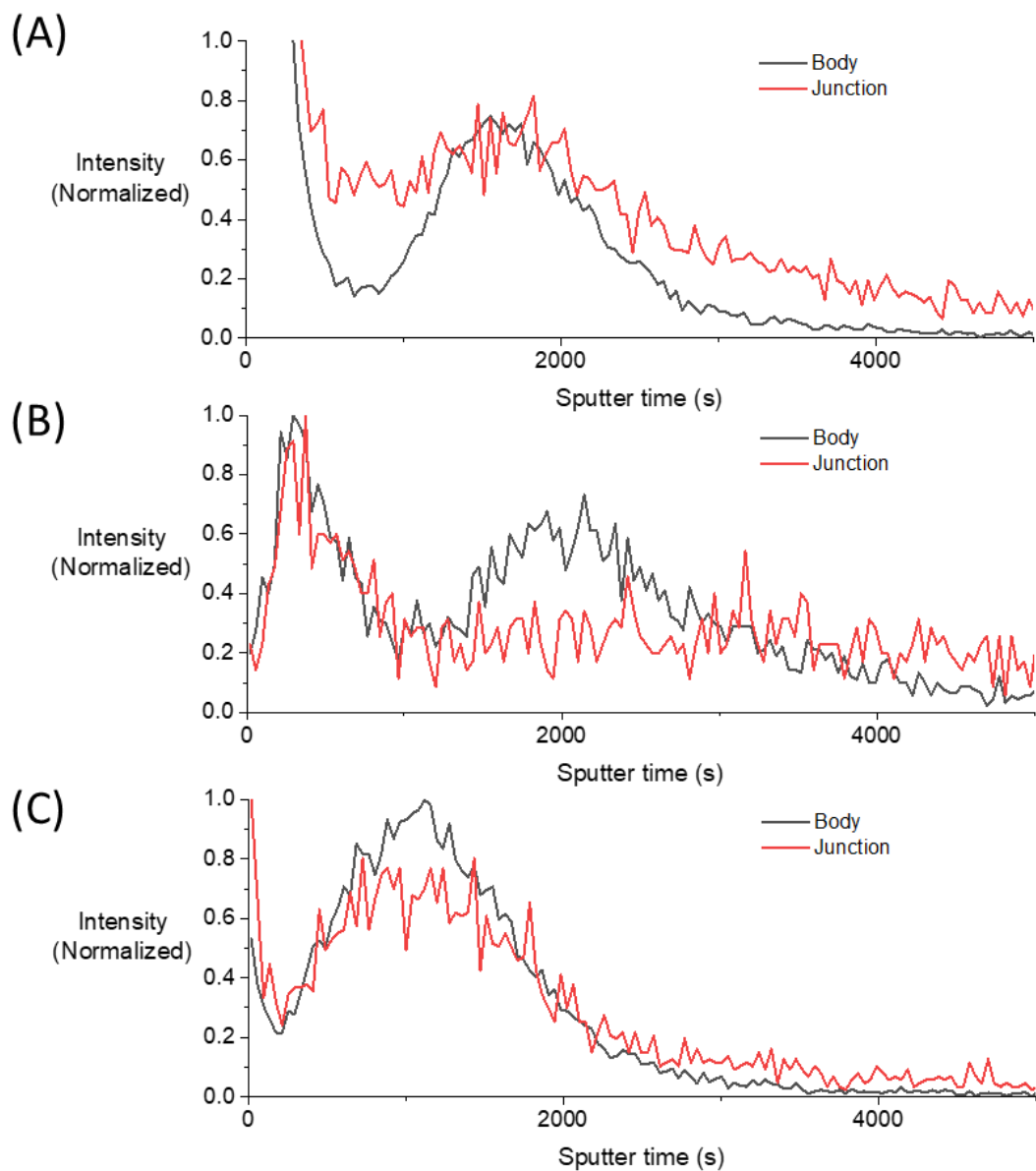


Figure S4: Comparison of three typical trends at the body and junction.

(A) Amino acid fragment  $C_4H_8N^+$ , (B)  $Ni^+$  and (C) a carbohydrate fragment ( $CHO^+$ ). The first peak of Ni at both body and the junction are situated at the same depth, possibly because the conductive fibers run across cells. Relative presence of amino acid fragments is higher between the top and bottom sheath at the junction compared to the body, and the rate of decrease in its intensity after the peak is slower at the junction.

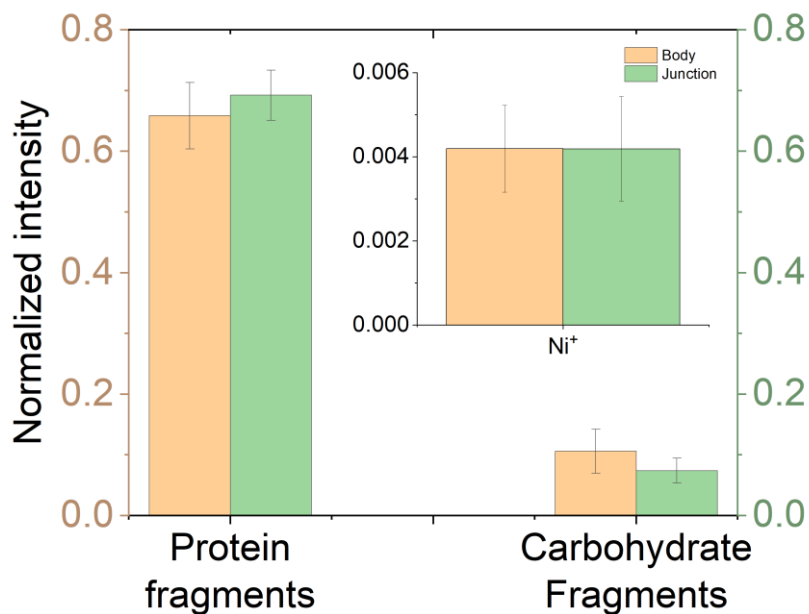


Figure S5: Comparison of protein-related, carbohydrate-related fragments and Ni at the body and junction.

Intensities are normalized by dividing the sum of identified protein fragments, carbohydrate fragments and Ni signal with the intensity of all the identified fragments given in tables S2-S6. The error bar given is on the basis of three measurements. Cell junctions have relatively more protein fragments compared to cell body, whereas an inverse relation exists for carbohydrate fragments. Ni is identical in both parts, indicating that Ni is not present within the junction.

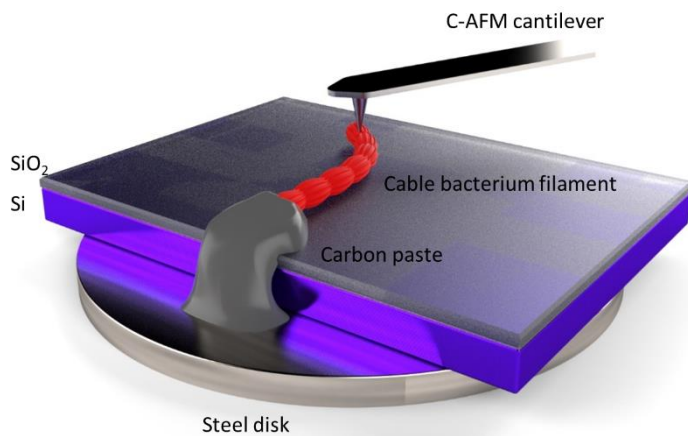


Figure S6: Schematic of conductive AFM setup.

A filament is placed over a Si wafer with 200 nm thick SiO<sub>2</sub> layer. One end of the filament is connected to the steel disk, which in turn sits on the AFM stage to which the bias voltage is applied, and the C-AFM cantilever is conductive and is connected to the ground of the controller, completing the electrical connection. When the tip sits on an exposed area of the filament, a current flows between the steel disk, through the filament to the cantilever. This is done for every pixel, resulting in the height and current images in Figure 5.

Table S1: Depth measurements of Ni<sup>+</sup> signal, CHO<sup>+</sup> signal and thickness of filament measured at the center of cell body. Depth values were obtained by a linear fit of AFM data as described in figure 6.

Sample No.	Ni <sup>+</sup> peak (nm)	CHO <sup>+</sup> peak (nm)
1	12.3	33.4
2	12.7	67.6
3	11.4	32.1
4	11.4	45.8
5	11.2	45.3

Table S2: Fragments associated with protein layer

ToF-SIMS assignment	Center Mass	Expected Mass (HCB)	Expected Mass (FI - DE)	Resolution (HCB)	Resolution (FI - DE)	Descriptor*	Used in PCA (HCB)	Used in PCA (FI - DE)
NH_3+	17.026	17.026	17.025	5934	1542		+	+
NH_4+	18.035	18.036	18.035	3557	1757			
C_2H_3+	27.023	27.023	27.021	5518	1752			
CH_2N+	28.019	28.019	28.020	5252	1538	G	+	+
C_2H_4+	28.031	28.030		5029				
CH_3N+	29.026	29.026		6121				
C_2H_5+	29.040	29.040	29.039	5158	1816			
CH_4N+	30.035	30.036	30.035	4614	1655	DERM SHYFK LG	+	+
CH_5N+	31.042	31.042		6389				
C_3H_5+	41.040	41.040	41.039	5406	1881			
C_2H_4N+	42.035	42.035	42.036	5881	1745	AF	+	+
CH_3N_2+	43.030	43.029		7399		R	+	
C_2H_5N+	43.042	43.041		6559				
CH_2NO+	44.014	44.012	44.013	8429	2622	N	+	+
CH_4N_2+	44.037	44.037		7481		R	+	
C_2H_6N+	44.052	44.052	44.049	5038	1665	ALFYH SMKD E	+	+
C_4H_2+	50.015	50.015		6919				
C_4H_3+	51.023	51.023	51.022	6446	2054		+	+
C_4H_5+	53.040	53.040	53.038	5859	2101			
C_3H_4N+	54.034	54.035		6636				
C_3H_3O+	55.020	55.020	55.013	5759	2450			
C_3H_6N+	56.056	56.052	56.049	5231	1815	FKM	+	+
C_3H_8N+	58.068	58.068	58.064	5302	1765	E	+	+
C_3H_7O+	59.050	59.051	59.048	5687	1887			
CH_6N_3+	60.058	60.059	60.054	5369	1831	R	+	+
C_2H_5S+	61.010	61.012		6039		M		
C_5H_5+	65.040	65.039	65.036	6535	2035			
C_4H_6N+	68.053	68.053		5204		P	+	
C_4H_5O+	69.036	69.037		5487		T		
C_5H_9+	69.074	69.073		5296		O		
C_3H_4NO+	70.034	70.033		5136		P	+	

C_4H_8N+	70.071	70.073	70.065	4293	1883	P	+	+
C_4H_10N+	72.086	72.088	72.076	4977	1847	V	+	+
C_2H_7N_3+	73.065	73.065	73.069	6295	1738	R		
C_3H_8NO+	74.067	74.066	74.066	5217	1992	T	+	+
C_5H_6N+	80.053	80.053	80.047	5451	1935	P	+	+
C_4H_7N_2+	83.061	83.058	83.051	3927	1750	V	+	+
C_4H_6NO+	84.048	84.049		5344		EQ	+	
C_5H_10N+	84.087	84.090		4724		K	+	
C_5H_12N+	86.104	86.104		5252		IL	+	
C_4H_10N_3+	100.089	100.088		5468		R		
C_4H_8NO_2+	102.051	102.056		6174		E Y (aromatic amino acid)		
C_7H_7O+	107.047	107.054	107.050	6027	1923		+	+
C_5H_8N_3+	110.080	110.082	110.063	4664	1617	RH F (aromatic amino acid)		
C_8H_10N+	120.086	120.087	120.063	6113	1721	W (aromatic amino acid)	+	+
C_9H_8N+	130.067	130.068	130.056	6862	1948			
C_8H_10NO+	136.090	136.080	136.053	6029	1596		+	+

Table S3: Ni signal

ToF-SIMS assignment	Center Mass	Expected Mass (HCB)	Expected Mass (FI - DE)	Resolution (HCB)	Resolution (FI - DE)	Description	Used in PCA (HCB)	Used in PCA (FI - DE)
Ni+	57.935	57.934	57.936	7252	2073		+	+

Table S4: Fragments associated with polysaccharide layer

ToF-SIMS assignment	Center Mass	Expected Mass (HCB)	Expected Mass (FI - DE)	Resolution (HCB)	Resolution (FI - DE)	Description	Used in PCA (HCB)	Used in PCA (FI - DE)
O+	15.995	15.995	15.989	6070	1942			
OH+	17.002	17.002	16.997	7223	1614			
H_3O+	19.019	19.019	19.017	4276	1839		+	+
CHO+	29.002	29.002	29.000	5580	2087		+	+
CH_2O+	30.010	30.010	30.005	6145	3098		+	+
CH_3O+	31.021	31.019	31.016	5418	2106		+	+
C_2H_2O+	42.010	42.010	42.003	6902	3305		+	+
C_3H_5O+	45.035	57.036	57.034	6300	2463		+	+
C_2H_5O_2+	61.031	61.031		6476			+	
C_3H_3O_2+	71.010	73.031	71.005	7071	2953		+	+
C_3H_5O_2+	73.030	71.016		6287			+	
CHO_2Na_2+	90.980	90.986	90.973	3034	2364			
C_4H_2O_2Na+	104.999	104.998		3860				

Table S5: Other general fiber sheath fragments

ToF-SIMS assignment	Center Mass	Expected Mass (HCB)	Expected Mass (FI - DE)	Resolution (HCB)	Resolution (FI - DE)	Description	Used in PCA (HCB)	Used in PCA (FI - DE)
H+	1.007	1.007		1901				
C+	12.000	11.999	11.997	5167	1622			
CH+	13.007	13.007	13.004	6237	1474			
N+	14.003	14.002		4137				
CH <sub>2</sub> +	14.015	14.015	13.004	6178	1474			
NH+	15.010	15.010		12287				
CH <sub>3</sub> +	15.023	15.024	15.023	4493	1665			
NH <sub>2</sub> +	16.018	16.018	16.024	5650	981			
C <sub>2</sub> H <sub>2</sub> +	26.015	26.014	26.011	5950	1652		+	+
CHN+	27.010	27.010		7510				
P+	30.974	30.973	30.964	5779	813	Poly-P, DNA, RNA		
C <sub>3</sub> H <sub>2</sub> +	38.015	38.015	38.013	6914	1705			
C <sub>2</sub> H <sub>3</sub> O+	43.019	43.019		5501				
C <sub>3</sub> H <sub>7</sub> +	43.056	43.055	43.055	5537	2380			
CHS+	44.980	44.979	44.984	7218	1912	C		
C <sub>2</sub> H <sub>5</sub> O+	45.035	45.035	45.039	6103	1713			
PO+	46.969	46.968		6815		Poly-P, DNA, RNA		
C <sub>3</sub> HO+	53.002	53.003	52.997	6562	2510			
C <sub>4</sub> H <sub>7</sub> +	55.057	55.056	55.054	5462	1823			
Fe+	55.935	55.934		7458		<sup>54</sup> Fe, <sup>56</sup> Fe	+	
C <sub>4</sub> H <sub>9</sub> +	57.071	57.071	57.077	4840	2939			
C <sub>2</sub> H <sub>3</sub> S+	58.990	58.995	59.001	8191	3131	C		
Cu+	62.929	62.929	62.922	8395	4696	<sup>63</sup> Cu, <sup>65</sup> Cu	+	+
CH <sub>2</sub> N <sub>2</sub> O <sub>2</sub> +	74.013	74.015	74.011	6330	1839			
C <sub>6</sub> H <sub>3</sub> +	75.024	75.025	75.022	6227	2132			
C <sub>6</sub> H <sub>5</sub> +	77.040	77.038	77.036	6444	1981			
C <sub>6</sub> H <sub>6</sub> +	78.043	78.042	78.038	4137	2047			
C <sub>3</sub> H <sub>7</sub> N <sub>2</sub> O+	87.050	87.053		4764		N		
C <sub>3</sub> H <sub>6</sub> NO <sub>2</sub> +	88.016	88.047		5521		D		
C <sub>7</sub> H <sub>7</sub> +	91.055	91.055	91.051	6277	2031			
C <sub>4</sub> H <sub>4</sub> NO <sub>2</sub> +	98.022	98.029		5629		N		
C <sub>4</sub> H <sub>7</sub> N <sub>2</sub> O <sub>2</sub> +	115.053	115.052	115.047	5486	1963	G		

Table S6: Fragments likely derived from medium, wafer and sediment matrix

ToF-SIMS assignment	Center Mass	Expected Mass (HCB)	Expected Mass (FI - DE)	Resolution (HCB)	Resolution (FI - DE)	Description	Used in PCA (HCB)	Used in PCA (FI - DE)
Na+	22.990	22.990	22.992	5216	1594	Salt		
Mg+	23.984	23.984	23.984	6281	1459	Salt, Sediment mineral		
Al+	26.982	26.981	26.981	6740	1604	Sediment mineral		
Si+	27.977	27.976	27.973	6651	1049	Sediment mineral		
K+	38.966	38.965	38.968	5344	1863	Salt		
Ca+	39.962	39.961	39.963	6814	1678	Salt, Sediment mineral		
NaCl+	57.958	57.954		11936		Salt		
KNa+	61.953	61.952		4007		Salt		
Na <sub>2</sub> O+	61.975	61.978		4569		Salt		
Na <sub>2</sub> OH+	62.985	62.985		4737		Salt		
NaO <sub>3</sub> H+	71.985	71.984	71.986	6426	1844	Salt		
KNaOH+	78.959	78.954	78.952	3869	2272	Salt		
Na <sub>2</sub> Cl+	80.952	80.963		7416		Salt		
K <sub>2</sub> NaSO <sub>4</sub> +	196.869	196.891		6328		Salt		
Au+	196.968	196.966	196.934	8734	1010	Wafer		
Au <sub>3</sub> +	590.901	590.890		10176		Wafer		